PAPER

Hybrid quantum-classical polarizability model for single molecule biosensing†

Ekaterina Zossimova, [ID] *[a,b] Johannes Fiedler, [ID] [c] Frank Vollmer[a] and Michael Walter [ID] [b,d,e]

Optical whispering gallery mode biosensors are able to detect single molecules through effects of their polarizability. We address the factors that affect the polarizability of amino acids, which are the building blocks of life, *via* electronic structure theory. Amino acids are detected in aqueous environments, where their polarizability is different compared to the gasphase due to solvent effects. Solvent effects include structural changes, protonation and the local field enhancement through the solvent (water). We analyse the impact of these effects and find that all contribute to an increased effective polarizability in the solvent. We also address the excess polarizability relative to the displaced water cavity and develop a hybrid quantum-classical model that is in good agreement with self-consistent calculations. We apply our model to calculate the excess polarizability of 20 proteinogenic amino acids and determine the minimum resolution required to distinguish the different molecules and their ionised conformers based on their polarizability.

1 Introduction

In the pursuit of developing biosensors with high spatial and temporal resolution, many new techniques have been invented to detect things that would otherwise not be visible to the naked human eye. A subclass of these techniques do not rely on images at all – instead they exploit the resonant properties of optical whispering gallery modes (WGM) to detect single molecules[1–3] down to 13-mer oligonucleotides[4,5] and Ångström-sized amino acids.[6] Molecules interacting with the biosensing field perturb the stable resonance of the WGM, and the magnitude of the perturbation is recorded as a signal, encoding information about the characteristic properties of target molecules.

Amino acids are the building blocks for proteins that are central for living systems. It is essential to understand how to categorise and potentially differentiate amino acids[7] using optical biosensors due to their diverse applications in healthcare, environmental monitoring, biotechnology, and scientific research.[8,9] Amino acids are particularly sensitive to solvent effects due to their amphoteric behaviour. At low pH, the amino group (–NH_2) acts as a base and accepts a proton from the solvent. At high pH, the carboxyl group (–COOH) donates a proton to the surrounding medium.

Within first-order perturbation theory, the shift of the WGM resonance is proportional to the dipole polarizability of the molecule in excess of the displaced solvent,[10] *i.e.* the excess polarizability of the molecule α_{ex}^*. Numerous methods exist to calculate the gasphase polarizability α of molecules, including additive atomistic models,[11,12] electronic structure methods[13,14] and machine learning algorithms[15–17] as the polarizability is central for the understanding of *e.g.* weak van der Waals interactions.[18–20] However, it is not so obvious how to transform $\alpha \rightarrow \alpha_{ex}^*$ when the molecule is in a solvent[21,22] due to several screening and field enhancement effects.[23,24] Developing an accurate model for α_{ex}^* can help to decode the biosensor signals and improve the specificity of polarizability-based biosensing techniques.

Density functional theory (DFT) is a quantum-mechanical method that is used to calculate molecular properties from their electronic density. DFT intrinsically accounts for molecular charge and can be conveniently combined with implicit solvent models to study solvated single molecules where the solvent is modelled as a continuum.[25–27] The inclusion of solvent effects is essential as the protonation state of the

[a]Department of Physics and Astronomy, Living Systems Institute, University of Exeter, EX4 4QD Exeter, UK. E-mail: ez216@exeter.ac.uk
[b]Freiburg Center for Interactive Materials and Bioinspired Technologies (FIT), University of Freiburg, D-79110 Freiburg, Germany
[c]Department of Physics and Technology, University of Bergen, Allégaten 55, 5007 Bergen, Norway
[d]Cluster of Excellence livMatS @ FIT, Freiburg, Germany
[e]Fraunhofer IWM, MikroTribologie Centrum μTC, Freiburg, Germany

amino acid can be expected to affect its polarizability. Previous studies have shown that implicit solvent models are able to describe the relative energetic stability of different conformers and protonation states of molecules in aqueous environments.[28–31]

Here, we model the solvation shell encompassing the molecule as a smooth cavity[32] to obtain optimised solvated structures of 20 proteinogenic amino acids, including their different protonation states. The smooth cavity model does not distinguish between the externally applied field and the local field seen by the solute molecule. The local fields are required to calculate α_{ex}^* and can be included using the classical Onsager model.[33] This leads to a self-consistent equation for the polarizability that must be solved numerically.[24] Alternatively, we also propose a hybrid quantum-classical model for α_{ex}^* that combines DFT calculations for molecular polarizability (without local field corrections) and scattering effects through a 3-layer cavity model for finite-sized particles. We implement both approaches in GPAW DFT code[34,35] and find that they give comparable results for α_{ex}^*. However, the hybrid quantum-classical model outperforms the numerical model in terms of computational speed and efficiency.

2 Effective polarizability model

The dipole polarizability α of a molecule describes the magnitude of the induced dipole moment due to an applied electric field $\boldsymbol{F}$

$$\boldsymbol{\mu} = \boldsymbol{\mu}_0 + \alpha\boldsymbol{F}, \tag{1}$$

where $\boldsymbol{\mu}_0$ denotes the static dipole moment and $\boldsymbol{\mu}$ denotes the total dipole moment. α has the SI unit $C^2\ m^2\ J^{-1}$, but can be scaled by $(4\pi\varepsilon_0)^{-1}$ (ε_0 is vacuum permittivity) to get the unit of volume, which is often less cumbersome.[36] In general, α is an anisotropic second-rank tensor $[\alpha]$ and depends on the frequency of the applied field. Diagonalization of α allows us to define the isotropic polarizability,

$$\hat{\alpha} = \frac{1}{3}(\alpha_1 + \alpha_2 + \alpha_3) \tag{2}$$

and the fractional anisotropy (FA)

$$\mathrm{FA} = \left[\frac{(\alpha_1 - \alpha_2)^2 + (\alpha_1 - \alpha_3)^2 + (\alpha_2 - \alpha_3)^2}{2(\alpha_1^2 + \alpha_2^2 + \alpha_3^2)} \right]^{1/2}, \tag{3}$$

where α_1, α_2 and α_3 are the eigenvalues of $[\alpha]$. The fractional anisotropy is a number between 0 and 1, where 0 corresponds to a perfectly isotropic molecule, and increasing values indicate higher polarizability anisotropy.

The WGM laser typically probes molecules using near-infrared to visible light to avoid radiation damage on the molecular level.[2] The associated frequencies are well below the electronic excitations of amino acids,[37] such that we can consider their real-valued response functions in the electrostatic limit,[38] i.e. $\alpha(\omega_{WGM}) \approx \mathrm{Re}[\alpha(\omega \mapsto 0)] \equiv \alpha$. This defines the electronic static polarizability of the molecule, which should represent a good

approximation at the frequency of the exciting light.[22,39] We further assume that the molecules are very small compared to the wavelength of the WGM laser, such that the spatial variation of the biosensing field in the range of the molecule can be neglected.

Under these conditions, the linearity in the external field $\boldsymbol{F}$ allows us to calculate α as

$$\alpha_{ij} = \frac{[\Delta\boldsymbol{\mu}(\boldsymbol{F})]_i}{F_j} = \frac{[\boldsymbol{\mu}(\boldsymbol{F})]_i - [\boldsymbol{\mu}_0]_i}{F_j} \tag{4}$$

where $\Delta\boldsymbol{\mu}$ is the change in the molecular dipole moment due to a finite electric field $\boldsymbol{F}$; i, j denoting the vector components. Eqn (4) is valid in the gasphase, where the local field acting on the molecule is the same as the external field.

There are changes for molecules in a solvent,[21,23,40,41] where the best model to describe these effects is not settled in the literature.[42] The influence of the solvent can be separated conceptually into two main factors:[22] first, the solvent affects the electron density of the molecules; second, it changes the local field $\boldsymbol{F}^L$ acting at the position of the molecule.[23,33] Generally, the effective polarizability within the solvent α^* is defined analogously to eqn (1) as[22]

$$\alpha_{ij}^* = \frac{[\Delta\boldsymbol{\mu}^*(\boldsymbol{F}^L)]_i}{F_j} \tag{5}$$

where the $*$ indicates effective values in the solvent and $\boldsymbol{F}$ is the external field applied outside of the solvent. The external field $\boldsymbol{F}$ is not the same as the local field $\boldsymbol{F}^L$ that the molecule experiences on the microscopic level as is made explicit in eqn (5).

3 Results and discussion

3.1 Solvent vs. gasphase polarizability

Amino acids are usually present in an aqueous environment. Therefore, this situation is most important. In order to understand the solvent effects on the polarizability of amino acids, it is nevertheless interesting to compare their gasphase polarizabilities to their corresponding polarizabilities within water using different approximations. Fig. 1 gives this comparison, where we observe first of all that α-gasphase occupies a range from 7.0 Å^3 for glycine (G) to 24.6 Å^3 for tryptophan (W). The gasphase FA is found in the range from 0.04 for lysine (K) to 0.33 for histidine (H$^+$).

Using α-gasphase as a reference, we can determine $\alpha_{g,ij}^{PCM} = [\Delta\boldsymbol{\mu}_g^{PCM}(\boldsymbol{F}^L)]_i/F_j^L$ within the polarizable continuum model (PCM) using the gasphase nuclear structure to isolate the effect of the solvent on the electronic density. Fig. 1a shows that this merely scales the gasphase polarizability by 9% consistently. The increase in the PCM polarizability compared to the gasphase is commonly found in the literature,[43,44] but was criticised by some authors.[45] The FA of the gasphase structures is not changed within the PCM, as shown by the green data points in Fig. 1b. The FA is thus solely caused by structural asymmetries within the molecule.

Fig. 1 (a) Solvent *vs.* gasphase polarizability of amino acids. α_g^{PCM}: polarizability of gasphase structures in the PCM solvent. α^{PCM}: polarizability of solvated structures in the PCM solvent. α^*: self-consistent polarizability with local field corrections. The dashed blue line shows the initial guess for α^* in the self-consistent calculation. The aqueous environment is described by the PCM with the optical permittivity of water. (b) Fractional anisotropy (FA) of solvated *vs.* gasphase amino acid structures in the PCM solvent. Most of the zwitterion structures have a larger polarizability anisotropy than their gasphase counterparts.

We next consider conformational and structural changes of the amino acids in water. Amino acids have charge-neutral functional groups in the gasphase, whereas these become ionised in the solvent. Most of the proteinogenic amino acids are zwitterions at physiological pH and several are either anions (aspartic acid, glutamic acid) or cations (arginine, lysine). The unbalanced charge distribution across the ionised conformers is more sensitive to the external field, resulting in a larger polarizability for the solvated *vs.* gasphase structures in the PCM solvent (α^{PCM} *vs.* α_g^{PCM} in Fig. 1a). The polarizability increase due to conformational change is approximately 5.5% on average, resulting in a total scaling factor of 1.15 relative to α-gasphase.

The conformational and structural changes also affect the FA, as shown by the orange data points in Fig. 1b. The solvated structures tend to have a higher polarizability anisotropy compared to the gasphase structures. Only histidine (H$^+$), aspartic acid (D$^-$, D) and leucine (L) show a lower fractional anisotropy for the solvated structures compared to the gasphase structures in the PCM solvent. These molecules correspond to the orange data points below the dashed identity line in Fig. 1b.

Finally, we have to consider changes in the local field due to the formation of a cavity around the solute molecule. This is not accounted for in our electronic structure calculations of α^{PCM}. We turn to a classical cavity model, originally formulated by Onsager,[33] to calculate the field enhancement within the cavity.

The solute molecule is described as a polarizable point dipole in the center of a spherical cavity with volume V. The solvent surrounding the cavity is described by the PCM with relative permittivity ε. The local field acting on the solute molecule can be represented as a superposition of a cavity field and reaction field, the latter of which depends recursively on the polarizability of the solute molecule. This leads to an equation for the local field enhancement, $\eta = F^L/F$, which can be written as[23,24,33]

$$\eta = \frac{3\varepsilon}{2\varepsilon + 1}\left[1 - \frac{8\pi(\varepsilon - 1)}{3(2\varepsilon + 1)}\frac{\alpha^*}{V}\right]^{-1},\qquad(6)$$

where we consider a spherically symmetric (averaged) α^* for simplicity. Eqn (6) is equivalent to $\eta = f^C(1 - f^R\chi^*)^{-1}$ in terms of the cavity field factor

$$f^C = \frac{3\varepsilon}{2\varepsilon + 1},\qquad(7)$$

the reaction field factor

$$f^R = \frac{8\pi(\varepsilon - 1)}{3(2\varepsilon + 1)},\qquad(8)$$

and the polarizability density of the molecule within the solvent $\chi^* = \alpha^*/V$.

We solve eqn (5) and (6) self-consistently. In the first step of the self-consistent cycle, we start with an initial guess for α^*

$$\alpha* \approx \alpha^{PCM}\eta^{PCM}\qquad(9)$$

where $\alpha_{ij}^{PCM} = [\Delta\boldsymbol{\mu}^{PCM}(\boldsymbol{F}^L)]_i/F_j^L$ and η^{PCM} is the field enhancement defined in eqn (6) with $\alpha^* = \alpha^{PCM}$. The dashed blue line in Fig. 1a shows the initial guess for α^* before the self-consistent calculation. We subsequently update η with the new value for α^* and iterate until the difference between sequential results for α^* is less than 1%. The results of the self-consistent calculation correspond to the blue data points in Fig. 1a. The best fit is quadratic because when $f^R\chi^* \to 0$, we can use a Taylor series expansion for η, which gives $\eta \approx f^C(1 + f^R\chi^*)$. Substituting η into eqn (9) leads to a cavity field term linear in α and a reaction field term quadratic in α.

3.2 Excess polarizability of amino acids

In experiments, the polarizability of target molecules is measured relative to the pure solvent. The pure solvent provides a baseline value for the polarizability measurement, and the molecule is detected by its polarizability in excess of the displaced solvent. In particular, in WGM experiments, the observed shift is caused by the change in polarizability when the resonator is in contact with the detected molecule instead of the omnipresent water.[5,6,46] We formulate two different models to calculate the excess polarizability of amino acids; the first uses our numerical results for $\alpha^\star$, and the second is a hybrid quantum-classical model inspired by a 3-layer cavity model in classical electromagnetism.

3.2.1 Numerical model.

A simple model for the excess polarizability involves comparing the polarizability densities of the solute molecule and the solvent, denoted by $\chi^\star$ and $\chi_w^\star$, respectively. We can express the excess polarizability $\alpha_{ex}^\star$ in terms of the polarizability densities as

$$\alpha_{ex}^\star = (\chi^\star - \chi_w^\star)V \tag{10}$$

where $\chi^\star = \alpha^\star/V$ and $\chi_w^\star = \alpha_w^\star/V_w$. Assuming that the solvent is water, we can calculate $\chi_w^\star$ by simulating a single explicit water molecule in an otherwise implicit background of water, following the self-consistent approach described above. The cavity volume of the solute molecule V and single explicit water molecule V_w can be calculated in GPAW using the Kirkwood–Buff method.[47] We find that $\chi_w^\star = 0.0613$ from numerical calculations.

We note that $\chi_w^\star$ can also be calculated analytically using the polarizability density of water from the Lorentz–Lorenz equation,

$$\chi_w = \frac{3}{4\pi}\left(\frac{\varepsilon - 1}{\varepsilon + 2}\right), \tag{11}$$

and the corresponding local field correction factor,

$$\eta_w = \frac{\varepsilon + 2}{3} \tag{12}$$

for a virtual cavity[23] (i.e. the local field enhancement when the solute molecule and solvent have the same polarizability density). The analytical formula can be written as $\chi_w^\star = \chi_w \eta_w$, which simplifies to

$$\chi_w^\star = \frac{\varepsilon - 1}{4\pi} \tag{13}$$

in terms of ε. The analytical result is $\chi_w^\star = 0.0613$ using the permittivity of water at optical frequencies, which is the same as our numerical result from the self-consistent calculation.

The results for the excess polarizability of amino acids using the self-consistent numerical model in eqn (10) are shown in Fig. 3a. Generally, the excess polarizability of the amino acids tends to be smaller than the gasphase polarizability, except for tryptophan, where the polarizability enhancement due to solvent effects overcompensates the negative contributions of the displaced water (see Fig. S2 in ESI†).

3.2.2 Hybrid quantum-classical model.

An alternative way to consider local field corrections is inspired by a classical 3-layer cavity model.[21] We consider the cavity shown in Fig. 2a, where the molecule is modelled as a finite-size hard sphere with radius R and permittivity ε_s. The hard sphere is surrounded by a vacuum shell, and the background medium is water with permittivity ε. The radius of the cavity encompassing the molecule and vacuum shell is R_c. We can define the polarizability of the hard sphere using the Lorentz–Lorenz equation as

$$\alpha_s = R^3\left(\frac{\varepsilon_s - 1}{\varepsilon_s + 2}\right) \tag{14}$$

and the excess polarizability of the cavity as

$$\alpha_c^\star = \varepsilon R_c^3\left(\frac{1 - \varepsilon}{1 + 2\varepsilon}\right). \tag{15}$$

Note, that the polarizabilities defined in eqn (14) and (15) are scaled by a factor of $(4\pi\varepsilon_0)^{-1}$ to get volumetric units.

The polarizability can be derived from the viewpoint of the field as a scattering process at the outer boundary of a multi-layer cavity using the scattering Green function for a spheri-

Fig. 2 (a) Classical 3-layer model to describe a finite-size molecule inside a cavity. The molecule is modelled as a hard sphere (shown in red), surrounded by a vacuum layer (black) and water as the background medium (blue). (b) The hard sphere is replaced by a real molecule with polarizability α^{PCM}, calculated using density functional theory. The cavity is determined by the shape of the molecule and is not necessarily spherical.

cally layered system.[48,49] This leads to an equation for the excess polarizability, given by[21]

$$\alpha_{ex}^* = \alpha_c^* + \alpha_s \left(\frac{3\varepsilon}{2\varepsilon+1}\right)^2 \left[1 + \frac{2\alpha_c^* \alpha_s}{R_c^6 \varepsilon}\right]^{-1} \quad (16)$$

in the classical picture.

We can replace the hard sphere in the classical model with a real molecule as shown in Fig. 2b. In doing so, we substitute the polarizability of the molecule without local field corrections α^{PCM} for α_s in eqn (16) and show that

$$\alpha_{ex}^* = \left(\chi^{PCM} \eta^{PCM} - \chi_w \eta_w\right) f^C V \quad (17)$$

in the hybrid quantum-classical picture. Here, we use $\chi^{PCM} = \alpha^{PCM}/V$ and $\eta^{PCM} = f^C(1 - f^R \chi^{PCM})^{-1}$, where f^C and f^R are defined in eqn (7) and (8), respectively. $\chi_w \eta_w$ is the same as χ_w^* in eqn (13). We can use $R_c^3 = 3V/4\pi$ to convert between the cavity radius and volume.

The numerical model in eqn (10) and the hybrid quantum-classical model in eqn (17) give very similar results for the excess polarizability, as shown in Fig. 3a. The benefit of using eqn (17) is that the excess polarizability is expressed in terms of χ^{PCM}, which is less computationally expensive to calculate than the self-consistent polarizability density χ^* that appears in eqn (10). For the set of 20 amino acids considered here, it takes approximately 7 iterations of the self-consistent equation to converge the result for α^*. Therefore, the calculation of χ^{PCM} is approximately 7 times faster than χ^*, on average.

Returning to eqn (17), we can define the *excess* polarizability density as $\chi_{ex}^* = \alpha_{ex}^*/V$. We can express eqn (17) as a quadratic polynomial in terms of χ^{PCM} by using a Taylor series expansion for η^{PCM} in the limit of small $f^R \chi^{PCM}$ as $\eta^{PCM} \approx f^C(1 + f^R \chi^{PCM})$. This lets us express χ_{ex}^* in powers of χ^{PCM} as

$$\chi_{ex}^* = \left[\frac{1-\varepsilon}{4\pi} + f^C \chi^{PCM} + f^C f^R \left(\chi^{PCM}\right)^2\right] f^C. \quad (18)$$

The quadratic equation for χ_{ex}^* agrees very well with the amino acids data, as shown in Fig. 4. χ_{ex}^* is generally smaller than χ^{PCM} in the range $0.00 < \chi^{PCM} < 0.12$, although the two quantities become comparable as χ^{PCM} increases due to the approximately quadratic scaling of the reaction field term. The excess polarizability density of water is zero since water is the background medium.

3.2.3 Detection of amino acids. The distinguishability of target molecules, and correspondingly the specificity of the biosensor, depends on whether there is a resolvable difference in the values of α_{ex}^*, assuming that the binding site of the molecule can be well controlled in experiments. The polarizability roughly correlates with the molecular volume, as shown in Fig. 3b. Glycine (G) is the smallest molecule studied and has the lowest excess polarizability; tryptophan (W) is the largest molecule studied and has the highest excess polarizability. Assuming that the biosensing field has the same intensity at the position of both molecules, we would expect glycine to produce the smallest shift in the biosensor signal and tryptophan the largest. The biosensor would need to resolve a polarizability difference of approximately 20 Å^3 to distinguish the two molecules with extreme polarizabilities. Other molecules, such as cysteine (C) and lysine (K$^+$) would be more difficult to resolve based on α_{ex}^*, despite the significant difference in cavity volume.

Fig. 3 (a) Comparison between the numerical model and hybrid quantum-classical model for the excess polarizability of amino acids. The results are plotted as a function of the cavity volume. (b) The excess polarizability for different protonation states (or net charge) of the amino acids.

Fig. 4 Solid blue line: quadratic approximation for the excess polarizability density, see eqn (18). Dotted blue line: linear approximation for the excess polarizability density (no reaction field, $f^R = 0$). The reference values for water are shown as orange dashed lines for comparison [$\chi_w = 0.0488$ from the Clausius−Mossotti relation in eqn (11)].

3.3 Effect of molecular charge

Biosensing experiments are often performed in a phosphate or a carbonate buffer, which stabilise different pH ranges. Amino acids have highly ionizable functional groups that can exchange protons with the surrounding water.[31] The number of protons exchanged depends on the pK_a values of the functional groups and on the availability of protons, *i.e.* the pH of the solution. It can be expected that the removal of a proton leads to an increase of the polarizability as the number of electrons responsible for the polarizability does not change, but they are less bound due to the lower nuclear charge. The hybrid quantum-classical model indeed predicts that negative charged molecules (anions) have a larger polarizability and that positively charged molecules (cations) have a lower polarizability compared to their charge neutral counterparts. This effect can be seen in Fig. 3b for aspartic acid (D), glutamic acid (E), histidine (H), lysine (K) and arginine (R).

We use glutamic acid as an example to compare how other polarizability models consider the effect of charge. Glutamic acid plays an important role in neuroscience, the food industry (*e.g.* monosodium glutamate), and energy production in the body where glutamate is involved in various metabolic pathways. Glutamic acid has two carboxyl groups (pK_1 = 2.13, pK_2 = 4.31) and an amine group (pK_3 = 9.67).[50] The net charge of glutamic acid is $q = -1$ at physiological pH but can vary between $q = +1$ in a highly acidic environment (fully protonated) and $q = -2$ in a highly alkaline environment (fully deprotonated). The actual protonation state for a given pH can be evaluated using the Henderson–Hasselbalch equation[51–53] as detailed in ESI†.

Optimised structures of solvated glutamic acid ions are used to compare different polarizability models in describing the effect of pH in Fig. 5. The direct DFT calculation through the hybrid quantum-classical model shows the expected behav-

iour of increasing polarizability with increasing charge. This effect cannot be captured with additive atomistic models, such as the Thole model,[11] because there the molecular polarizability always scales with the number of atoms only. The AlphaML (B3LYP) machine learning algorithm also cannot capture this effect because it has been trained on a dataset of neutral molecules,[54,55] where the effect of charge would not be evident. The polarizability difference between conjugate acid–base pairs in these atomistic (and machine learning) models is roughly equal to the polarizability of a hydrogen atom $\alpha_H = 0.7$ Å^3, but no hydrogen atoms are removed from the amino acids in reality. The hybrid model thus finds a much larger polarizability difference between conjugate acid–base pairs (between 1.7–2.5 Å^3) with the opposite charge dependence.

4 Conclusions

We have shown that amino acid polarizabilities in the solvent are enhanced as compared to gasphase counterparts, due to different structures, different charge, and most importantly local field enhancements. We have developed a self-consistent excess polarizability model based on finite field polarizabilities determined in a continuum solvent model. We furthermore showed that the computationally less demanding hybrid excess polarizability model proposed in eqn (17) leads to very similar results.

Our results will help to decode the signals from single molecule biosensing experiments, where it is important to accurately quantify the excess polarizability of single molecules. The solute molecule can be identified through α_{ex}^* by measuring the magnitude of the biosensor signals. The fractional anisotropy can also be used to identify single molecules by measuring the shift ratio between transverse electric (TE) and transverse magnetic (TM) modes.[56–58] Some of the molecules, such as cysteine (C), asparagine (N) and valine (V), may be hard to distinguish based on α_{ex}^* alone. However, the TE to TM shift ratio provides a second molecular fingerprint to help differentiate and categorise the biosensor signals. The shift ratio is expected to be larger for a molecule with high anisotropy and can be referenced against the fractional anisotropy data† to help identify the target molecules. The results presented here form a guide on the experimental sensitivity required to differentiate between different amino acids using WGM-based biosensors. The methods presented can also be applied to other molecules that are of physiological significance.

Fig. 5 Polarizability of glutamic acid as a function of pH. The hybrid quantum-classical calculation includes solvent effects and is sensitive to the electronic density of the molecule. The Thole model[11] is an additive atomistic model and can only capture the effect of adding or removing a hydrogen atom between conjugate acid–base pairs. The machine learning algorithm[15,16] (AlphaML) has not been trained on charged molecules and captures the same effect as the Thole model.

5 Computational details

We obtain the gasphase structures of amino acids from the NOMAD repository,[59] where we use the structures published by Ropo *et al.*[60] as a starting point to generate the corresponding solvated conformers. We start with the subset of 1694 calcium-coordinated structures provided there and remove the divalent
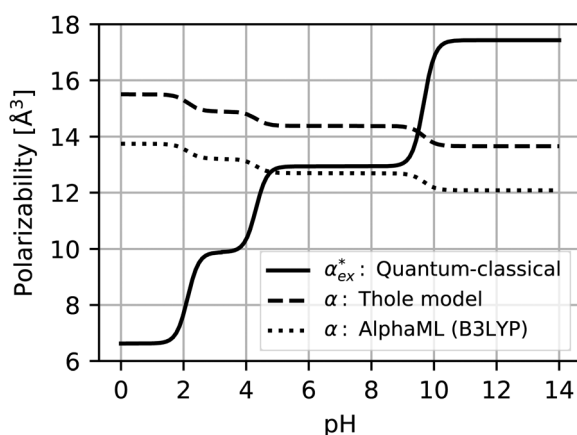
calcium ion to generate a set of initial structures. We use the cation-coordinated structures, as opposed to the bare gasphase structures, to obtain a mix of initial structures that resemble zwitterionic and non-zwitterionic conformers. Sampling a range of initial structures is important because the relaxation algorithm converges to the nearest local minimum in the energy landscape, which may not be representative of the global energetic minimum.

The electronic structure of the molecules is described with the GPAW DFT package.[34,35,61] The electron density and Kohn–Sham states are described within the projector augmented wave (PAW) method, where the smooth parts are represented on real space grids. The grid spacing in the simulation is 0.2 Å for representing the smooth wavefunctions within the PAW description. The size of the simulation box ensures that each atom is at least 4 Å away from its boundary. We use the PBE exchange–correlation functional[62] in the calculation of the DFT energy. The aqueous environment is described by the polarizable continuum model (PCM).[32]

The amino acid conformers are relaxed using the Broyden–Fletcher–Goldfarb–Shanno algorithm as implemented in the atomic simulation environment (ASE)[63] until the maximal force on each atom is below 0.05 eV Å^{-1}, corresponding to the structure of the molecule in the next local minimum of the energy landscape. Here, we use the static permittivity of water ($\varepsilon_{stat} = 78.36$)[64] in the ground state DFT calculations. The resulting amino acid conformers are sorted according to their relative energies. We consider different protonation states separately, since the net charge can fluctuate depending on the pH of the buffer solution. We find that charge neutral amino acids prefer the zwitterionic form in an aqueous environment. We further consider different protonation states of arginine (R), lysine (K), histidine (H), glutamic acid (E) and aspartic acid (D), which exist predominantly in their ionised form at neutral pH. We use the lowest energy conformers in the polarizability calculations and note the minor variation due to different gasphase and solvated conformers, see Fig. S4 and S5 in ESI,† respectively.

The molecular polarizabilities are calculated from eqn (4) using the finite-field method with external field strength $|\boldsymbol{F}| = 0.01$ V Å^{-1}. This field strength is tested to be sufficiently small to avoid higher-order contributions and still large enough to avoid numerical difficulties.[65] The calculation using finite fields does not have convergence issues in contrast to perturbation theory approaches (see ESI† for the comparison between linear response time-dependent DFT (TDDFT)[66] and the finite field method). We apply the same approach to calculate the polarizability in an aqueous environment α^{PCM} using eqn (5) and the local field strength, $|\boldsymbol{F}^{L}| = \eta|\boldsymbol{F}|$. Here, we use the optical permittivity of water ($\varepsilon_{opt} = 1.77$)[67] in the solvation model for the calculation of α^{PCM} because the biosensor typically probes the molecules at optical to near-infrared frequencies, where the permittivity of water is equal to the squared refractive index.

Our description relies on the application of the PCM, which does not account for explicit water molecules that may interact with and stick to charged groups of the amino acids. Such situations can be modelled by including explicit water molecules within the solute region.[68,69] However, including explicit water molecules raises the question of how to separate the polarizability of the amino acids from that of the attached water molecules. Wannier orbitals may be a solution,[70,71] but this approach largely influences the calculated polarizabilities (see Table S3 in ESI†). Furthermore, we note that an implicit description of the solvent is consistent with the 3-layer cavity model that is used to describe the scattering of the fields (see Fig. 2), where the background medium is represented by its permittivity, ε. It is not immediately clear how this description has to be adjusted in the case of additional explicit water molecules. Answering these questions is beyond the scope of the presented work and has to be assigned to future investigations.

Author contributions

E. Z., M. W. and J. F. conceptualised the excess polarizability models. E. Z. and M. W. developed the code to calculate the excess polarizability and wrote the original draft of the manuscript. E. Z. collected and visualised the data. F. V. and M. W. acquired funding for the project and all authors contributed to review and edit the manuscript.

Conflicts of interest

There are no conflicts to declare.

Acknowledgements

Notes and references

1 F. Vollmer and S. Arnold, *Nat. Methods*, 2008, **5**, 591–596.
2 N. Toropov, G. Cabello, M. P. Serrano, R. R. Gutha, M. Rafti and F. Vollmer, *Light: Sci. Appl.*, 2021, **10**, 42.
3 D. Yu, M. Humar, K. Meserve, R. C. Bailey, S. N. Chormaic and F. Vollmer, *Nat. Rev. Methods Primers*, 2021, **1**, 83.

4 M. D. Baaske, M. R. Foreman and F. Vollmer, *Nat. Nanotechnol.*, 2014, **9**, 933–939.

5 N. Eerqing, S. Subramanian, J. Rubio, T. Lutz, H.-Y. Wu, J. Anders, C. Soeller and F. Vollmer, *ACS Photonics*, 2021, **8**, 2882–2888.

6 S. Vincent, S. Subramanian and F. Vollmer, *Nat. Commun.*, 2020, **11**, 2043.

7 H. Ouldali, K. Sarthak, T. Ensslen, F. Piguet, P. Manivet, J. Pelta, J. C. Behrends, A. Aksimentiev and A. Oukhaled, *Nat. Biotechnol.*, 2020, **38**, 176–181.

8 A. M. Pettiwala and P. K. Singh, *Curr. Med. Chem.*, 2018, **25**, 2272–2290.

9 H. Kosakamoto, N. Okamoto, H. Aikawa, Y. Sugiura, M. Suematsu, R. Niwa, M. Miura and F. Obata, *Nat. Metab.*, 2022, **4**, 944–959.

10 S. Arnold, M. Khoshsima, I. Teraoka, S. Holler and F. Vollmer, *Opt. Lett.*, 2003, **28**, 272.

11 B. T. Thole, *Chem. Phys.*, 1981, **59**, 341–350.

12 L. S. Booth, E. V. Browne, N. P. Mauranyapin, L. S. Madsen, S. Barfoot, A. Mark and W. P. Bowen, *Sci. Rep.*, 2022, **12**, 1995.

13 S. Millefiori, A. Alparone, A. Millefiori and A. Vanella, *Biophys. Chem.*, 2008, **132**, 139–147.

14 L. H. R. D. Santos, A. Krawczuk and P. Macchi, *J. Phys. Chem. A*, 2015, **119**, 3285–3298.

15 D. M. Wilkins, A. Grisafi, Y. Yang, K. U. Lao, R. A. DiStasio and M. Ceriotti, *Proc. Natl. Acad. Sci. U. S. A.*, 2019, **116**, 3401–3406.

16 Y. Yang, K. U. Lao, D. M. Wilkins, A. Grisafi, M. Ceriotti and R. A. DiStasio, *Sci. Data*, 2019, **6**, 152.

17 C. Feng, J. Xi, Y. Zhang, B. Jiang and Y. Zhou, *J. Chem. Theory Comput.*, 2023, 1207–1217.

18 A. Tkatchenko and M. Scheffler, *Phys. Rev. Lett.*, 2009, **102**, 073005.

19 R. A. DiStasio, V. V. Gobre and A. Tkatchenko, *J. Phys.: Condens. Matter*, 2014, **26**, 213202.

20 S. Y. Buhmann, *Dispersion Forces I – Macroscopic Quantum*, Springer, 2012, vol. 247.

21 J. Fiedler, P. Thiyam, A. Kurumbail, F. A. Burger, M. Walter, C. Persson, I. Brevik, D. F. Parsons, M. Boström and S. Y. Buhmann, *J. Phys. Chem. A*, 2017, **121**, 9742–9751.

22 J. Fiedler, M. Walter and S. Y. Buhmann, *J. Chem. Phys.*, 2021, **154**, 104102.

23 A. Aubret, M. Orrit and F. Kulzer, *ChemPhysChem*, 2019, **20**, 345–355.

24 R. Wortmann and D. M. Bishop, *J. Chem. Phys.*, 1998, **108**, 1001–1007.

25 J. Tomasi, B. Mennucci and R. Cammi, *Chem. Rev.*, 2005, **105**, 2999–3094.

26 G. Fisicaro, L. Genovese, O. Andreussi, S. Mandal, N. N. Nair, N. Marzari and S. Goedecker, *J. Chem. Theory Comput.*, 2017, **13**, 3829–3845.

27 S. Ringe, N. G. Hörmann, H. Oberhofer and K. Reuter, *Chem. Rev.*, 2022, **122**, 10777–10820.

28 D. L. Crittenden, M. Chebib and M. J. T. Jordan, *J. Phys. Chem. A*, 2004, **108**, 203–211.

29 M. Targema, N. O. Obi-Egbedi and M. D. Adeoye, *Comput. Theor. Chem.*, 2013, **1012**, 47–53.

30 F. Comitani, K. Rossi, M. Ceriotti, M. E. Sanz and C. Molteni, *J. Chem. Phys.*, 2017, **146**, 145102.

31 R. Ghassemizadeh, B. Moore, T. Momose and M. Walter, *J. Phys. Chem. B*, 2019, **123**, 4392–4399.

32 A. Held and M. Walter, *J. Chem. Phys.*, 2014, **141**, 174108.

33 L. Onsager, *J. Am. Chem. Soc.*, 1936, **58**, 1486–1493.

34 J. J. Mortensen, L. B. Hansen and K. W. Jacobsen, *Phys. Rev. B: Condens. Matter Mater. Phys.*, 2005, **71**, 035109.

35 J. Enkovaara, C. Rostgaard, J. J. Mortensen, J. Chen, M. Dułak, L. Ferrighi, J. Gavnholt, C. Glinsvad, V. Haikola, H. A. Hansen, H. H. Kristoffersen, M. Kuisma, A. H. Larsen, L. Lehtovaara, M. Ljungberg, O. Lopez-Acevedo, P. G. Moses, J. Ojanen, T. Olsen, V. Petzold, N. A. Romero, J. Stausholm-Møller, M. Strange, G. A. Tritsaris, M. Vanin, M. Walter, B. Hammer, H. Häkkinen, G. K. H. Madsen, R. M. Nieminen, J. K. Nørskov, M. Puska, T. T. Rantala, J. Schiøtz, K. S. Thygesen and K. W. Jacobsen, *J. Phys.: Condens. Matter*, 2010, **22**, 253202.

36 P. W. Atkins and R. S. Friedman, *Molecular Quantum Mechanics*, OUP, Oxford, 2011.

37 R. Maul, M. Preuss, F. Ortmann, K. Hannewald and F. Bechstedt, *J. Phys. Chem. A*, 2007, **111**, 4370–4377.

38 J. Fiedler, K. Berland, J. W. Borchert, R. W. Corkery, A. Eisfeld, D. Gelbwaser-Klimovsky, M. M. Greve, B. Holst, K. Jacobs, M. Krüger, D. F. Parsons, C. Persson, M. Presselt, T. Reisinger, S. Scheel, F. Stienkemeier, M. Tømterud, M. Walter, R. T. Weitz and J. Zalieckas, *Phys. Chem. Chem. Phys.*, 2023, **25**, 2671–2705.

39 M. Walter and M. Moseler, *J. Chem. Theory Comput.*, 2020, **16**, 576–586.

40 S. Pipolo, S. Corni and R. Cammi, *J. Chem. Phys.*, 2014, **140**, 164114.

41 R. Cammi, *J. Comput. Chem.*, 2019, **40**, 2309–2317.

42 J. Fiedler, D. F. Parsons, F. A. Burger, P. Thiyam, M. Walter, I. Brevik, C. Persson, S. Y. Buhmann and M. Boström, *Phys. Chem. Chem. Phys.*, 2019, **21**, 21296–21304.

43 M. M. Alam, V. Kundi and P. P. Thankachan, *Phys. Chem. Chem. Phys.*, 2016, **18**, 21833–21842.

44 W. Liang, X. Li, L. R. Dalton, B. H. Robinson and B. E. Eichinger, *J. Phys. Chem. B*, 2011, **115**, 12566–12570.

45 M. Medved', Š. Budzák, W. Bartkowiak and H. Reis, *Handbook of Computational Chemistry*, Springer International Publishing, Cham, 2017, pp. 741–794.

46 J. Topolancik and F. Vollmer, *Biophys. J.*, 2007, **92**, 2223–2229.

47 J. G. Kirkwood and F. P. Buff, *J. Chem. Phys.*, 1951, **19**, 774–777.

48 L.-W. Li, P.-S. Kooi, M.-S. Leong and T.-S. Yee, *IEEE Trans. Microwave Theory Tech.*, 1994, **42**, 2302–2310.

49 M. S. Tomaš, *Phys. Rev. A*, 2001, **63**, 053811.

50 *CRC Handbook of Chemistry and Physics*, ed. W. M. Haynes, CRC Press, 2014.

51 L. J. Henderson, *Am. J. Physiol.*, 1908, 173–179.

52 K. Hasselbalch, *Die Berechnung der Wasserstoffzahl des Blutes aus der freien und gebundenen Kohlensäure desselben, und die Sauerstoffbindung des Blutes als Funktion der Wasserstoffzahl*, Julius Springer, 1916.

53 P. A. Sims, *J. Chem. Educ.*, 2010, **87**, 803–808.

54 L. C. Blum and J.-L. Reymond, *J. Am. Chem. Soc.*, 2009, **131**, 8732.

55 G. Montavon, M. Rupp, V. Gobre, A. Vazquez-Mayagoitia, K. Hansen, A. Tkatchenko, K.-R. Müller and O. A. von Lilienfeld, *New J. Phys.*, 2013, **15**, 095003.

56 I. Teraoka, S. Arnold and F. Vollmer, *J. Opt. Soc. Am. B*, 2003, **20**, 1937.

57 I. Teraoka and S. Arnold, *J. Opt. Soc. Am. B*, 2006, **23**, 1381.

58 I. Teraoka and S. Arnold, *J. Appl. Phys.*, 2007, **101**, 023505.

59 M. Ropo, C. Baldauf and V. Blum, NOMAD Repository Entry, 2015, https://nomad-lab.eu/prod/v1/gui/dataset/doi/10.17172/NOMAD/20150526220502.

60 M. Ropo, M. Schneider, C. Baldauf and V. Blum, *Sci. Data*, 2016, **3**, 160009.

61 J. J. Mortensen, A. H. Larsen, M. Kuisma, A. V. Ivanov, A. Taghizadeh, A. Peterson, A. Haldar, A. O. Dohn, C. Schäfer, E. O. Jónsson, E. D. Hermes, F. A. Nilsson, G. Kastlunger, G. Levi, H. Jónsson, H. Häkkinen, J. Fojt, J. Kangsabanik, J. Sødequist, J. Lehtomäki, J. Heske, J. Enkovaara, K. T. Winther, M. Dulak, M. M. Melander, M. Ovesen, M. Louhivuori, M. Walter, M. Gjerding, O. Lopez-Acevedo, P. Erhart, R. Warmbier, R. Würdemann, S. Kaappa, S. Latini, T. M. Boland, T. Bligaard, T. Skovhus, T. Susi, T. Maxson, T. Rossi, X. Chen, Y. L. A. Schmerwitz, J. Schiøtz, T. Olsen, K. W. Jacobsen and K. S. Thygesen, GPAW: open Python package for electronic-structure calculations, *arXiv*, 2023, preprint, arXiv:2310.14776 [cond-mat, physics:physics], DOI: **10.48550/arXiv.2310.14776**.

62 J. P. Perdew, K. Burke and M. Ernzerhof, *Phys. Rev. Lett.*, 1996, **77**, 3865–3868.

63 A. H. Larsen, J. J. Mortensen, J. Blomqvist, I. E. Castelli, R. Christensen, M. Dułak, J. Friis, M. N. Groves, B. Hammer, C. Hargus, E. D. Hermes, P. C. Jennings, P. B. Jensen, J. Kermode, J. R. Kitchin, E. L. Kolsbjerg, J. Kubal, K. Kaasbjerg, S. Lysgaard, J. B. Maronsson, T. Maxson, T. Olsen, L. Pastewka, A. Peterson, C. Rostgaard, J. Schiøtz, O. Schütt, M. Strange, K. S. Thygesen, T. Vegge, L. Vilhelmsen, M. Walter, Z. Zeng and K. W. Jacobsen, *J. Phys.: Condens. Matter*, 2017, **29**, 273002.

64 M. Uematsu and E. U. Franck, *J. Phys. Chem. Ref. Data*, 1980, **9**, 1291–1306.

65 D. Porezag and M. R. Pederson, *Phys. Rev. B: Condens. Matter Mater. Phys.*, 1996, **54**, 7830–7836.

66 M. Walter, H. Häkkinen, L. Lehtovaara, M. Puska, J. Enkovaara, C. Rostgaard and J. J. Mortensen, *J. Chem. Phys.*, 2008, **128**, 244101.

67 G. M. Hale and M. R. Querry, *Appl. Opt.*, 1973, **12**, 555.

68 D. Himmel, S. K. Goll, I. Leito and I. Krossing, *Chem. – Eur. J.*, 2011, **17**, 5808–5826.

69 O. Brügner, T. Reichenbach, M. Sommer and M. Walter, *J. Phys. Chem. A*, 2017, **121**, 2683–2687.

70 P. L. Silvestrelli and M. Parrinello, *Phys. Rev. Lett.*, 1999, **82**, 3308–3311.

71 J. J. Molina, S. Lectez, S. Tazi, M. Salanne, J.-F. Dufrêche, J. Roques, E. Simoni, P. A. Madden and P. Turq, *J. Chem. Phys.*, 2011, **134**, 014511.